

Polygonal patterns of cyclones on Jupiter: Convective forcing and anticyclonic shielding

Andrew Ingersoll (✉ api@gps.caltech.edu)

California Institute of Technology <https://orcid.org/0000-0002-2035-9198>

Shawn P. Ewald

California Institute of Technology

Federico Tosi

Istituto Nazionale di AstroFisica

Alberto Adriani

Istituto Nazionale di AstroFisica

Alessandro Mura

Istituto Nazionale di AstroFisica

Davide Grassi

Istituto Nazionale di AstroFisica

Christina Plainaki

Agenzia Spaziale Italiana

Giuseppe Sindoni

Agenzia Spaziale Italiana

Cheng Li

University of Michigan

Lia Siegelman

Scripps Institution of Oceanography

Patrice Klein

California Institute of Technology

William R. Young

Scripps Institution of Oceanography

Article

Keywords: Jupiter, Juno, vortex, convection, atmosphere

Posted Date: May 11th, 2021

DOI: <https://doi.org/10.21203/rs.3.rs-388198/v1>

License:  This work is licensed under a Creative Commons Attribution 4.0 International License.

[Read Full License](#)

Version of Record: A version of this preprint was published at Nature Astronomy on September 22nd, 2022. See the published version at <https://doi.org/10.1038/s41550-022-01774-0>.

1 Polygonal patterns of cyclones on Jupiter:
2 Convective forcing and anticyclonic shielding
3

4 Andrew P. Ingersoll^{a,1}, Shawn P. Ewald^a, Federico Tosi^b, Alberto Adriani^b, Alessandro Mura^b, Davide
5 Grassi^b, Christina Plainaki^c, Giuseppe Sindoni^c, Cheng Li^d, Lia Siegelman^e, Patrice Klein^f, William R.
6 Young^e
7

8 ^aPlanetary Science, California Institute of Technology, 1200 E. California Blvd, Pasadena, CA 91125,
9 USA

10 ^bIstituto Nazionale di AstroFisica – Istituto di Astrofisica e Planetologia Spaziali (INAF-IAPS), Rome, Italy

11 ^cAgenzia Spaziale Italiana (ASI), Via del Politecnico snc, 00133 - Rome, Italy

12 ^dClimate and Space Sciences and Engineering, University of Michigan, 2455 Hayward Street, Ann Arbor,
13 MI 48109, USA

14 ^eScripps Institution of Oceanography, University of California, San Diego, La Jolla, CA 92037, USA
15

16 ^fEnvironmental Science and Engineering Department, Geological and Planetary Sciences Division,
17 CALTECH, 1200E California Blvd, Pasadena CA 91125, USA
18

19 ¹**Corresponding author:** Andrew P. Ingersoll, 626-376-6872, api@gps.caltech.edu

20 **ORCID**S registered at PNAS by individual authors

21 **Author Contributions:** API led the research and wrote the document. SPE did the data analysis and
22 prepared the figures. FT prepared the geometric tables that were used in the analysis. Others oversaw
23 the successful functioning of the JIRAM instrument and provided expertise on using it for image
24 processing. CL, LS, PK and WRY provided expertise on vortices.

25 **Competing Interest Statement:** No competing interests

26 **Keywords:** Jupiter, Juno, vortex, convection, atmosphere

27 **This PDF file includes:**

28 **Main Text:** Introduction, Results, Discussion, Methods

29 Figures 1 to 4

30 Tables: none
31

32 **Abstract**

33 From its unique pole-to-pole orbit, the Juno spacecraft discovered cyclones arranged in
34 polygonal patterns around the poles of Jupiter. In a related modeling study the stability of the
35 pattern depends on shielding -- a ring of anticyclonic vorticity surrounding each cyclone.
36 Without shielding the vortices merge. Here we present high-resolution measurements obtained
37 by tracking clouds in sequences of infrared images. There is vorticity of both signs at 200-km
38 scales. The standard deviation is 0.32 times the vorticity of a large cyclone, whose relative
39 vorticity is 0.46 times the planetary vorticity. Shielding exists at large scales, and it has the
40 magnitude and distance from the vortex center predicted in the model. There is horizontal
41 divergence of both signs at 200-km scales, with standard deviation 0.64 times the vorticity
42 standard deviation. We propose that these intense structures are convection and that convection
43 is the principal energy source for the large vortices.

44 **Significance Statement**

45 Vorticity is the local rate of spin. For large-scale, slowly-varying flows in atmospheres and
46 oceans, the spin of the planet is greater than that of the flow and is therefore a controlling factor.
47 The vortices at Jupiter's poles are particularly interesting because they are arranged in geometric
48 patterns that endure for years. Such patterns have been seen in laboratory experiments and
49 theoretical models but never before in a planetary atmosphere. With a 10-fold increase in spatial
50 resolution, we have discovered a world seething with intense small-scale activity. The interaction
51 of this world with the large vortices resembles a food chain, with convection bringing energy up
52 from below. Studying these exotic atmospheric structures helps us understand vortex behavior in
53 general.

54

55 At Jupiter's north pole there are eight cyclones that form an octagon, with one cyclone at
56 each vertex and one additional cyclone in the center^{1 2}. The centers of the cyclones are at
57 latitudes of $83 \pm 1^\circ$, which is about 8700 km from the pole. Jupiter's south pole is the same
58 except there are only five cyclones that form a pentagon and one at the center, with vertices at
59 latitudes of $-83 \pm 1^\circ$. The polygons and the individual vortices that comprise them have been
60 stable for four years of observation³⁴. The observations are taken every 53 days over a 1-2 hour
61 period at perijove, which is the spacecraft's closest approach to Jupiter. The peak azimuthal wind
62 speeds around each vortex range from 70 to 100 m s⁻¹, and the radial distance from the peak to
63 the vortex center is about 1000 km⁵. The polygonal patterns rotate slowly, such that the vertices
64 in the south drift to the west at 0.04 m s⁻¹ and those in the north show no consistent drift³. The
65 cyclones perform small regular oscillations, but neither the merging nor the disappearance of any
66 cyclone has occurred⁶.

67
68 There have been only a handful of theoretical studies that specifically address the polar
69 cyclones on Jupiter and Saturn^{7 8 9 10 11}. Saturn's polar cyclones are fundamentally different
70 from Jupiter's because there is only one at each pole^{12 13}. Moreover, Saturn has a 160 m s⁻¹
71 zonal jet located at a latitude of -88.5° circling the south pole¹⁴. Saturn's north pole has not
72 been measured. In contrast, there are no zonal jets greater than 10 m s⁻¹ circling the poles of
73 Jupiter¹⁵. Saturn's northern hemisphere has a hexagon, which is a meandering zonal jet at 75°
74 whose six excursions in latitude give it a hexagonal shape^{16 17 18 19 20}. But the hexagon has no
75 closed-streamline structures, i.e., no vortices, and exists by a different mechanism from the polar
76 cyclones on Jupiter.

77
78 In a related modeling paper with some of the same authors, Li20⁷, we created cyclones
79 that have the observed gross properties - maximum velocity and radius, and arranged the
80 cyclones into polygonal patterns around the pole to see which ones are stable. This approach
81 reveals the importance of shielding - a ring of anticyclonic vorticity surrounding each of the
82 cyclones. Shielding is important in tropical meteorology. It determines whether tropical cyclones
83 merge, drift apart, or orbit each other²¹²²²³²⁴. In Li20 the radius of the anticyclonic ring divided
84 by the radius of maximum cyclonic velocity must be less than 4.5 in order to get a stable
85 pattern⁷. A larger ratio leads to merging and ultimately a single polar cyclone. Anticyclonic
86 vorticity is present in the models discussed earlier⁸⁹¹⁰¹¹, but apparently it does not organize into
87 shields that are strong enough to prevent merging.

88
89 In the present paper our measurement objective was to measure the velocity throughout
90 the north polar region at scales down to ~ 100 km. From the velocity field we would compute the
91 vertical component of vorticity and horizontal divergence. One goal was to look for shielding to
92 see if the theory of Li20 might apply to Jupiter. The other goal was simply to explore the hidden
93 world of small-scale motions. We found shielding, but we also discovered a world where
94 horizontal divergence and convergence rivaled the vorticity, and vorticity of both signs rivaled
95 that of the large-scale cyclones.

96 Scales of the Motion

97
98
99 The vertical component of vorticity due the planet's spin is $2\Omega\cos\theta$ and is called f , the
100 planetary vorticity, where Ω is the planetary rotation rate and θ is colatitude. The increase of f

101 with northward distance, $df/dy = 2\Omega\sin\theta/a$ is called β , where a is the radius of the planet. On
 102 Earth it causes cyclones to drift poleward²¹²². An important length scale at mid-latitudes is $L_\beta =$
 103 $(V/\beta)^{1/2}$, where V is a characteristic velocity. It roughly matches the widths of the zonal jets on
 104 Jupiter and Saturn²⁵²⁶²⁷²⁸. The length scale enters in criteria for zonal jet stability²⁹, and it is also
 105 the scale below which the flow is dominated by turbulence and above which it tends toward
 106 alternating zonal jets. With small-scale vortices as an initial condition, the flow evolves through
 107 a state of propagating waves and then tends toward alternating zonal jets³⁰. However, at the
 108 poles, where β tends linearly to zero, a length scale based on minus its gradient $\gamma = -d\beta/dy =$
 109 $2\Omega/a^2$ is more appropriate. The length scale is $L_\gamma = (V/\gamma)^{1/3}$, and for $V = 80 \text{ m s}^{-1}$ it is about
 110 10,500 km. L_γ represents the radius of the circle around the pole inside of which the effect of the
 111 vortices - turbulence -- is greater than the effect of β and the jets. Note that L_γ is the distance
 112 from a specific point -- the pole, and L_β is not. The value of L_γ is close to the 8700 km size of the
 113 polygons on Jupiter.

114
 115 The effect of deep winds on surface features is uncertain. The Juno gravity field indicates
 116 that the zonal winds extend from the surface down to the 3000 km level³¹. This statement only
 117 applies within $\pm 25^\circ$ of the equator, because the gravity wind experiment is not sensitive to
 118 higher latitudes³². And models of the deep winds show how they might affect the visible features
 119 ³³³⁴. But when one is varying parameters to fit data about specific features, it is wise to start
 120 simply. The shallow water (SW) equations have only two dependent variables, the horizontal
 121 velocity \mathbf{v} and the gravitational potential ϕ associated with the layer thickness, and they are
 122 functions only of the horizontal coordinates and time. A single layer of fluid of thickness h that
 123 floats hydrostatically on a much thicker fluid at rest is known as a 1.5-layer model. For this we
 124 have $\phi = g_r h$, where g_r is the reduced gravity -- the gravitational acceleration times the
 125 fractional density difference $\Delta\rho/\rho$ between the two layers²¹²². ϕ obeys the 2D continuity
 126 equation, and minus its horizontal gradient is the acceleration due to pressure. Potential vorticity
 127 (PV) is an important conserved quantity--a constant for each fluid element. For the SW equations
 128 PV is $(\zeta + f)/\phi$, where $\zeta = (\nabla \times \mathbf{v}) \cdot \hat{\mathbf{k}}$ is the relative vorticity -- the curl of the horizontal
 129 velocity.

130
 131 Rotation is dominant when the Rossby number $Ro = V/(fL)$ is small, where L is a
 132 characteristic length. For a jovian cyclone with $V = 80 \text{ m s}^{-1}$ and $L = 1000 \text{ km}$, one finds $Ro =$
 133 0.23. The ratio ζ/f is exactly twice this value. The radius of deformation $L_d = \sqrt{\phi/f}$ is the
 134 horizontal length scale over which the vortices interact. L_d is inversely proportional to the sine of
 135 latitude through the $1/f$ factor, and different assumptions about the vertical stratification put the
 136 average L_d at the poles in the range 350 - 1300 km⁷. This brackets the 1000-km radius of the

137 individual cyclones on Jupiter. If the velocity is fixed, Ro increases as L decreases, and
138 eventually rotation will not dominate the flow.

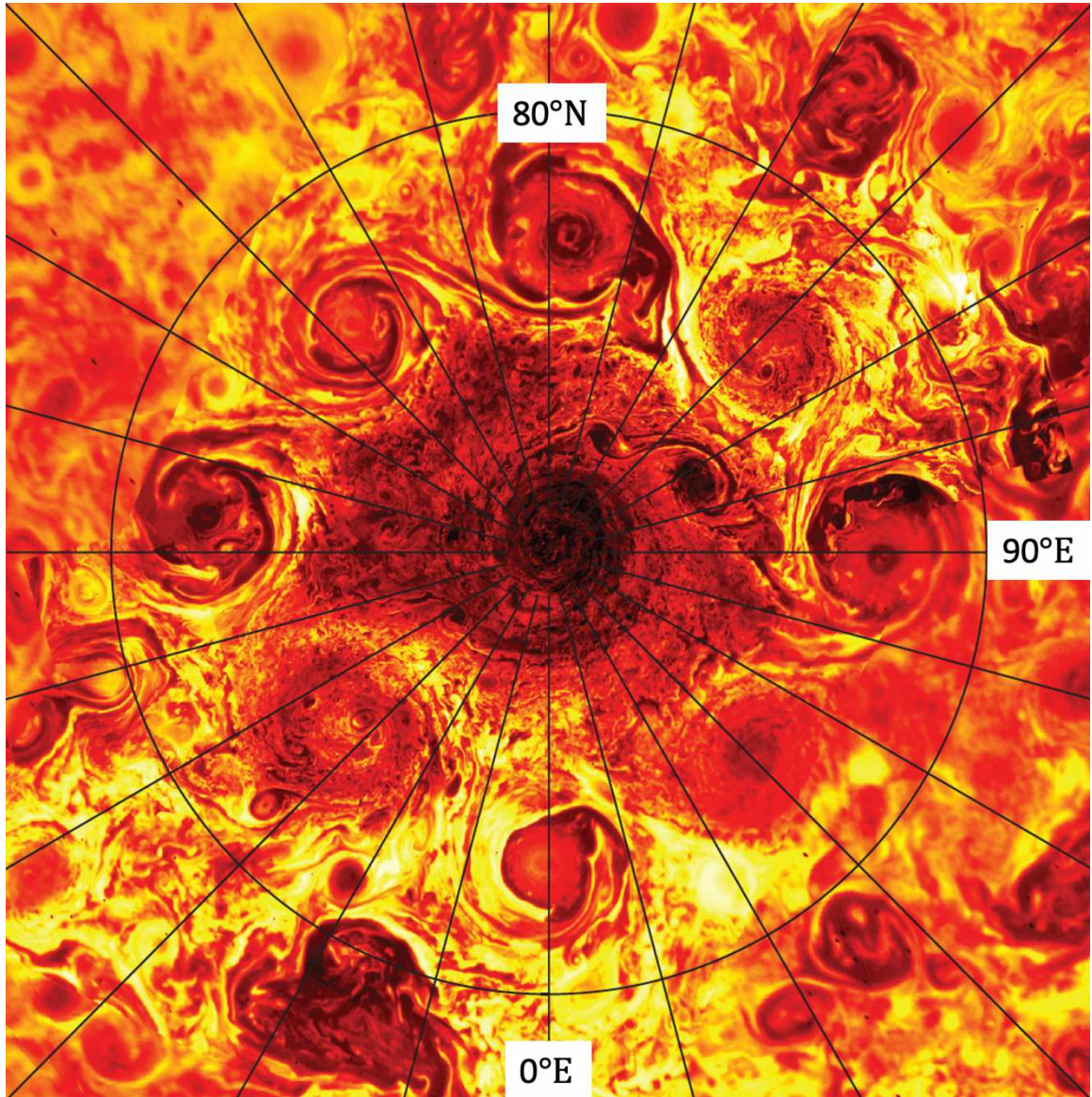
139

140

141 **Observations**

142

143



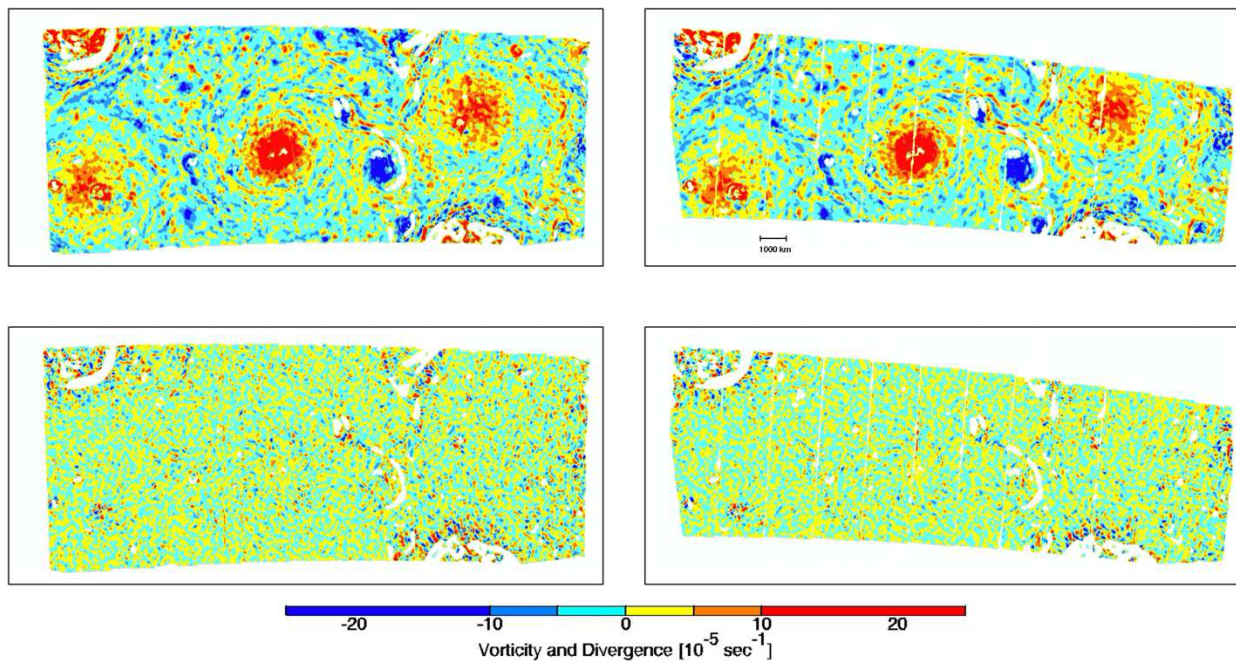
144

145

146 **Figure 1. Infrared image of the northern hemisphere as seen by JIRAM ². The circle at 80° latitude**
147 **is about 12,000 km from the pole. The radiances have been corrected for nadir viewing, with bright**
148 **yellow signifying greater radiance and dark red signifying lesser radiance. Because of these**
149 **corrections and the non-linearity of the Planck function, one can only say that the average**
150 **brightness temperature is somewhere in the range 215-220 K. The figures shown in this paper**
151 **cover the central cyclone and the two cyclones at 135° and 315° east longitude, respectively. The**
152 **two dark features at 120-150° east, whose filaments spiral toward their centers in a clockwise**
153 **direction, are anticyclones.**

154
155
156
157
158
159
160
161
162
163
164
165

Figure 1 shows the octagon of cyclones surrounding the north pole and describes the region covered by our vorticity and divergence maps. The maps show features in the clouds at scales down to ~ 100 km, which is much less than the 1000-km radius where the azimuthal velocity is greatest. The measurement requires tracking clouds in a pair of images separated in time to get velocity, and then taking closed line integrals to get vorticity and divergence. The maps are derived from infrared images taken by the Jupiter Infrared Auroral Mapper (JIRAM) on February 2, 2017³⁵. The JIRAM M filter tracks the clouds at 4.5-5.0 μm wavelength. A brightness anomaly indicates a hole in the upper cloud, allowing radiation from warmer, deeper levels to escape. Details of image processing are in the Methods section and in the Supplementary Information (SI).



166
167
168
169
170
171
172
173
174
175

Figure 2. Vorticity (top row) and divergence (bottom row) derived from two determinations of the wind field using separate data (left and right), termed n0103 and n0204. The long dimension of each rectangle is $\sim 20,000$ km, and the smallest features are ~ 100 km in diameter. Each determination is derived from a series, each of which consists of 12 adjacent images laid side by side. The seams between the 12 images are visible as faint vertical lines. The white spaces are regions where the image entropy³⁶ was below a threshold needed for reliable cloud-tracked wind analysis. They cover 1.8% and 2.1% of the pixels in the left and right maps, respectively. For further information, see the Methods section

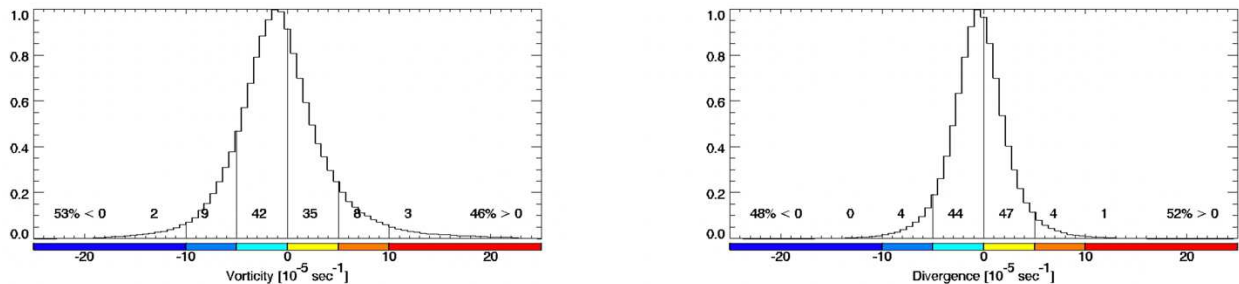
176
177
178
179
180
181
182
183

Figure 2 shows vorticity and divergence maps for two determinations of the wind field. A series of 12 images was started every 8 minutes to cover the same region at the north pole of Jupiter. The spacecraft was approaching Jupiter, and the image resolution changed from 22 km/pixel in the middle of the first series to 14 km/pixel in the middle of the fourth series, 24 minutes later. The two maps on the left were made by measuring cloud displacements between the first and third series, which are 16 minutes apart, and the two maps on the right were made from the second and fourth series, which are also 16 minutes apart. The left and right maps are separated in time by only 8 minutes, but they use entirely different images. The persistence and

184 movement of features, even those ~ 100 km in size, shows that the high-contrast, small-scale
 185 features are not measurement noise.

186 The small features move counterclockwise around the large cyclones and clockwise
 187 around the two anticyclones. This motion is visible when one blinks the left and right vorticity
 188 maps back and forth, as one can do with *fig_s1_polar_vortex_blink* in the SI. Even at the fastest
 189 speed, 80 m s^{-1} , the displacement over 8 minutes is only 38 km, which is ~ 2 times the resolution
 190 of the instrument. Notice that the central cyclone and the two cyclones at lower left and upper
 191 right almost disappear in the divergence maps, but the cyclones at upper left and lower right do
 192 not. The latter two cyclones are at 90° and 270°E in Figure 1. Their distinguishing characteristic
 193 is a lack of small-scale features, which are needed for accurate feature tracking. We used image
 194 entropy (Shannon entropy)³⁶ to confirm this visual impression, and chose an entropy threshold
 195 that covered up most but not all of the suspicious pixels in the divergence maps. Those pixels
 196 were not used either in the divergence or the vorticity data processing. The original images
 197 without the covering and histograms of the entropy are *fig_s2_entropy_masks_removed* in the SI.

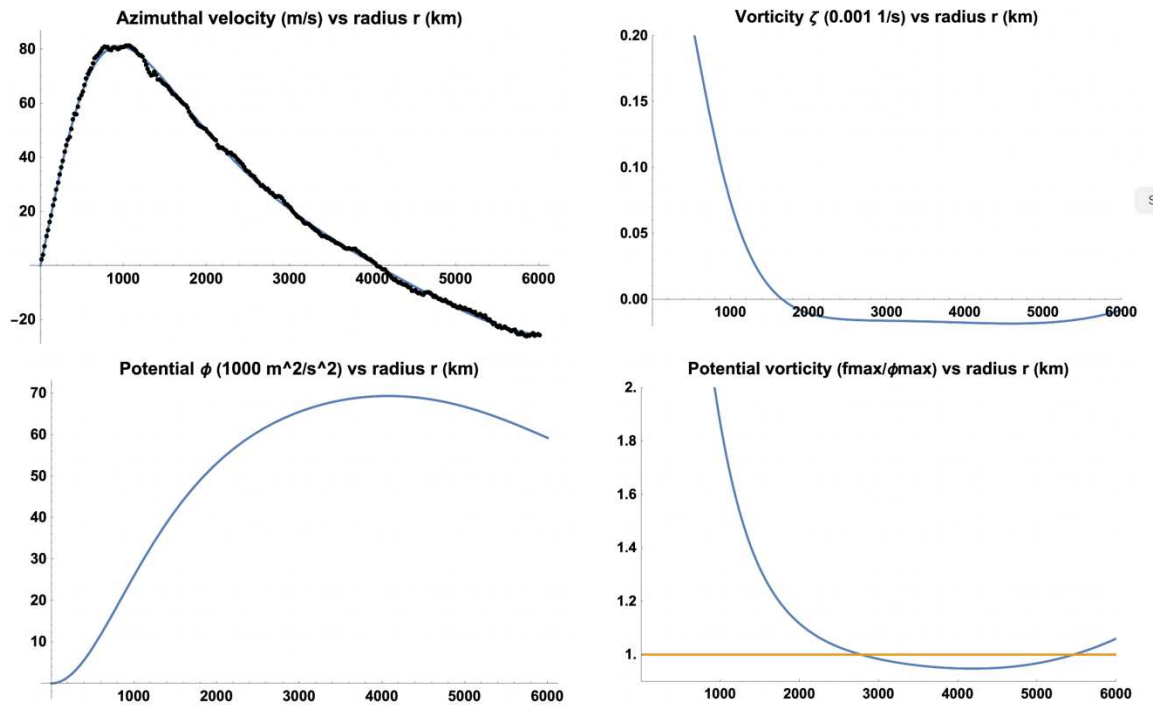
198 Figure 3 shows histograms of the points in Figure 2 and the percentages in each color bin.
 199 The standard deviations of vorticity and divergence are 5.1 and $3.25 \times 10^{-5} \text{ s}^{-1}$, respectively, but
 200 they have longer tails relative to the center than a normal distribution. The long tail of positive
 201 vorticity comes mostly from the central cyclone and extends out at least halfway to the planetary
 202 vorticity value $f = 2\Omega = 35 \times 10^{-5} \text{ s}^{-1}$. The long tail of negative vorticity comes mostly from the
 203 two anticyclones to the right of the central cyclone, but there are many smaller features with both
 204 positive and negative vorticity. The mean vorticity and mean divergence are 0.02 and 0.23 , both
 205 in units of 10^{-5} s^{-1} , respectively. Thus the mean values are much less than the standard deviations.
 206



207
 208
 209 **Figure 3. Histograms of vorticity (left) and divergence (right) for the maps shown in Figure 2. The**
 210 **vorticity and divergence scales are the same, and the colors are the same as those used in Figure**
 211 **2. The number above each color bin is the percentage of pixels in that bin.**

212 Figure 4 shows the azimuthal mean \bar{v} of the azimuthal velocity around the north central
 213 cyclone as a function of radius r out to 6000 km. Also shown are the mean vorticity $\bar{\zeta}$, the mean
 214 potential $\bar{\phi}$, and the mean potential vorticity $\bar{P}\bar{V}$. The curves are derived by a linear least squares
 215 fit to 5 smooth functions. Therefore they filter out the intense 100-km scale motions without
 216 affecting the description of motions on the scale of the cyclones and the region between them.
 217 The profile of $\bar{v}(r)$ agrees with earlier estimates⁵³, including the fact that the profile at $r > 2000$
 218 km falls off faster than $1/r$, implying negative vorticity in that region. See Methods for details on
 219 the fitting process.
 220

221 The profile of azimuthal velocity vs. radius yields a lower bound on the mean radius of
 222 deformation $L_d = \sqrt{\bar{\phi}}/f$. The potential ϕ in Figure 4 is computed from an integral and is therefore
 223 uncertain by an additive constant. However, $\phi = g_r h$ is proportional to the thickness, and the
 224 thickness cannot be negative. The figure is computed with $\phi = 0$ at the vortex center. The largest
 225 ϕ is $69,349 \text{ m}^2/\text{s}^2$ at $r = 4075 \text{ km}$, and it cannot be smaller there without ϕ becoming negative at
 226 the center. This gives $L_d = \sqrt{\bar{\phi}}/f = 749 \text{ km}$ as the lower bound for the radius of deformation,
 227 which is in the middle of estimates obtained from lower latitudes ⁷ taking into account the
 228 variation of f with latitude. We caution, however, that L_d is a fixed atmospheric parameter only
 229 for quasi-geostrophic (QG, or small Rossby number) motion, and Jupiter's polar cyclones are not
 230 fully QG, since $\zeta/f \sim 0.46$. In the shallow water equations, L_d describes the stratification far
 231 from any strong vortices and large pressure gradients.
 232



233
 234
 235
 236 **Figure 4. Mean azimuthal velocity and vorticity (top row) and mean gravitational potential**
 237 **and potential vorticity (bottom row). The fitted curve for velocity (blue) is almost covered**
 238 **by the data points (black). Potential vorticity is scaled by the planetary vorticity at the pole**
 239 **divided by the $r = 4075 \text{ km}$ peak value of ϕ , assuming it is equal to $L_d^2 f^2$ with $L_d = 1000 \text{ km}$.**
 240 **The variations of PV are not due to f , which decreases by only 0.35% from the pole to $r =$**
 241 **6000 km.**

244 To have stable polygons, Li20 requires an anticyclonic ring - shielding - around each
 245 cyclone ⁷. The distance from the center of each vortex to the annulus of minimum PV has to fall
 246 between ~ 2 and 4.5 times the radius of maximum azimuthal velocity, which is $\sim 1000 \text{ km}$. Recall
 247 that the vertices of the polygons average 8700 km from the pole. Figure 4 shows a broad annulus
 248 of negative vorticity at $1600 < r < 6000 \text{ km}$ with a minimum of $-1.83 \times 10^{-5} \text{ s}^{-1}$ at $r = 4591 \text{ km}$.

249 This is more than 5% of the planetary vorticity f at the pole but of opposite sign. The scaled PV
250 has a local minimum of 0.948 at $r = 4184$ km. This minimum is 2 or 3 times deeper than that
251 required by the model. The location of these minima agrees well with the model's ratio of 4.5 for
252 the minimum PV radius to the 1000-km radius of maximum velocity. All of this suggests that
253 large-scale shielding exists on Jupiter and is operating despite the small-scale activity.

254

255 Convection

256

257 A major scientific result of this paper is the large magnitude of vorticity and divergence
258 with both positive and negative sign at ~ 200 km scales. These properties point to convection, but
259 not the type of convection observed at lower latitudes. Severe thunderstorms on Earth have
260 diameters of 30-40 km³⁷³⁸. A hurricane is ~ 20 times larger³⁹. But the atmospheric scale height
261 on Jupiter is 5 times larger than on Earth, 40 km vs 8 km. So if the ratio of horizontal to vertical
262 dimensions is the same on the two planets, then jovian thunderstorms should have diameters of
263 150-200 km. This roughly matches the intense small-scale structures reported in this paper.

264

265 Divergence and convergence also point to convection. Horizontal divergence requires
266 vertical convergence and therefore vertical winds, which are defining elements of convection. If
267 a rising parcel conserves PV, then when it spreads out at the top of the atmosphere its $\zeta + f$
268 must decrease along with its h . Since f is a large positive quantity when the Rossby number is
269 small, and does not change as the parcel rises, the parcel's ζ must decrease by a large fractional
270 amount. In other words, rising parcels become anticyclones when they spread out at the top⁴⁰.
271 The opposite is also true: Upper-level convergence, which would accompany sinking parcels,
272 would lead to cyclonic vorticity at the top of the downwelling plume. The former describes
273 convection in Earth's atmosphere, where moist plumes rising from Earth's boundary layer
274 occupy $\sim 1\%$ of the area and slow sinking occupies the rest⁴⁰. The latter describes convection in
275 Earth's oceans, where cold sinking plumes break out of the mixed layer at the top of the ocean
276 and sink⁴¹. Lacking a solid surface below the clouds, Jupiter's atmosphere might have both
277 intense updrafts and intense downdrafts, which is consistent with equal amounts of divergence
278 of both signs. In other words, Jupiter's atmosphere might be behaving partly like an ocean⁴.

279

280 The ratio of divergence to vorticity at 150-300 scales also points to convection. In units
281 of 10^{-5} s^{-1} , the vorticity standard deviations are 5.1, both for images n0103 and n0204. The
282 corresponding divergence standard deviations are 3.4 and 3.1. The smaller values associated with
283 n0204 are probably due to the 20% better resolution of n0204 compared to n0103. For the large-
284 scale, slowly-varying cyclones compared to the planetary rotation (small Rossby number), one
285 expects small values for the ratio of divergence to vorticity, in any case no larger than ζ/f , which
286 is ~ 0.46 . This upper bound is based on terms in the vorticity equation. Intense, short-lived
287 convection like a terrestrial thunderstorm can have large convergence at the bottom and large
288 divergence at the top. Apparently the small structures that we see in Figures 2 and 3 are
289 intermediate between rotation-dominated and convection-dominated storms.

290

291 Although the large divergence suggests convection, the small-scale features in Figs. 2 do
292 not look like the lightning storms at lower latitudes, and both are obvious candidates for
293 convection. The imaging system on Galileo was able to pinpoint the sources of lightning by
294 following the clouds from day to night⁴²⁴³ over a 2-3 hour period. The storms range from 200 to

295 1600 km in size, are separated by 10^4 km in distance, and flash many times per minute. The
296 storms occur overwhelmingly in the belts, which are the cyclonic bands as defined by the
297 alternating eastward and westward jet streams. This seems to contradict evidence for upwelling
298 in the anticyclonic zones⁴⁴. The preference for belts could be due to thinning of the stably
299 stratified upper layers, which brings moisture-laden air up to its lifting condensation level⁴⁵⁴⁶.
300 Upwelling in the belts at cloud base and downwelling just below the tropopause is a real
301 possibility and an active area of study⁴⁷⁴⁸⁴⁹

302

303 Discussion

304

305 What to do next? On the observation side, we will pursue the brightness power spectrum
306 vs. spatial scale and the covariances of vorticity, divergence, and infrared brightness. The latter
307 has a resolution of ~ 16 km, and the derived divergence and vorticity have a resolution of ~ 100
308 km. Low brightness is an indicator of high clouds, which could be a sign either of upward
309 velocity or upward displacement. That effort is a separate paper and has been submitted⁵⁰. We
310 will study Jupiter's white ovals, which also have been observed by JIRAM⁵¹. On the theory side,
311 one should revisit the polar vortex models that are forced by small-scale convection⁸⁹¹⁰¹¹.
312 Although lacking a beta effect, there are models that produce large scale vortices from small-
313 scale convection in rapidly-rotating fluids⁵²⁵³, and that too should be pursued.

314

315

316 Methods

317

318 Table S1 in the SI gives the archival filenames and our working names for the 48 images
319 that were used in the analysis. The images are adjacent rectangular strips with 12 images per
320 series, and there are 4 series named n01 to n04, each of which records roughly the same place on
321 the planet 8 minutes after the one before. The size of each resolution element varies smoothly
322 from ~ 22 km/ pixel in the middle of n01 to ~ 14 km/pixel in the middle of n04. The first step in
323 the processing is to determine the precise location on the planet of each resolution element in
324 every image. This is done with NAIF/SPICE data from the spacecraft⁵⁴ and precise geometric
325 calibration of the JIRAM instrument³⁵. The second step is to map the brightness patterns onto a
326 grided reference plane tangent to the planet at the pole. That data is filename *data_s3_mapped*
327 *brightness* as part of the Supplementary Information (SI).

328

329 The third step is to measure cloud displacements in the reference plane using the
330 Tracker3 software from JPL. The software automatically searches for the best correlation of
331 brightness patterns between two images. This is done between images in series n01 and n03 and
332 between images in series n02 and n04. Velocity is the displacement in km divided by the time
333 interval, which is always close to 16 minutes but depends on which image in each series was
334 used. Correlation is done within a square box in the reference plane. After experimenting we
335 settled on 15 km/pixel in the reference plane and a 15 x 15 pixel correlation box for the Tracker3
336 software. In other words, we use a square 225 km on a side to define a feature. Therefore the
337 resolution of the wind measurement is ± 12.5 km. We oversample it by a factor of 2.5 to obtain
338 wind vectors on a 45 x 45 km grid. That data set is filename *data_s4_velocity vectors* in the SI.
Finally, we determine vorticity and divergence at every grid point by integrating around the 8

339 surrounding points using Stokes's theorem and Gauss's law, respectively. Those data are
 340 filename *data_s5_figure_2_data* in the SI.

341 The error in the velocity estimate σ_v depends crucially on the granularity of the scene at
 342 the scale of the resolution element δ , which on average is about 18 km. Except for no features at
 343 all, for which there is no estimate, the worst case is a single cloud feature of size $\leq \delta$, for which
 344 the variance $\sigma_v^2 = 2\delta^2/\Delta t^2$, where Δt is the 16-minute time step and the factor of 2 arises because
 345 we are subtracting position in two images. Then $\sigma_v = 2^{1/2}\delta/\Delta t$, about 26.5 m/s. However if the
 346 velocity measurement is the average of N statistically independent estimates of velocity, the
 347 variance is $2\delta^2/\Delta t^2/N$. The best case is when N is the number of resolution elements in the
 348 correlation box, which is L on a side such that $N = (L/\delta)^2$. Then $\sigma_v = 2^{1/2}\delta/\Delta t/N^{1/2} = 2^{1/2}\delta^2/L/\Delta t$,
 349 which is 2.1 m/s for $L = 225$ km.

350 A quantitative measure of granularity is image entropy H ³⁶. We define it for each 15 x 15
 351 correlation box from the histogram of brightness values in the box:

$$352 \quad H = -\sum p_k \log_2(p_k) \quad (1)$$

353 The input data are 32-bit numbers, but we only have 225 pixels. We divide the range from the
 354 brightest to the darkest pixel into 256 grey levels, and we count the number of times that each
 355 grey level appears in the image. That number divided by 225 is p_k , the frequency of occurrence
 356 of grey level k normalized so that $\sum p_k = 1$. The sum is over the 256 grey levels. If the
 357 brightness corresponding to a particular grey level k_1 does not occur in the image, then $p_{k_1} = 0$.
 358 At least 31 of the p_k 's must be zero. If all 225 pixels have brightness corresponding to grey level
 359 k_2 , then $p_{k_2} = 1$ and all the other p_k 's = 0, resulting in $H = 0$. If the brightness levels of all the 225
 360 pixels are different, then $H = \log_2(225) = 7.81$. This is the maximum entropy for this problem.
 361 Low entropy is bad for feature tracking, and we experimented to find a value that eliminated the
 362 most suspicious data, like the large pixel-to-pixel variations in the upper left and lower right
 363 corners of the divergence maps. We manually verified that the feature-tracking software was
 364 failing in those regions.

365 The data of Figure 4 consist of ~26,000 measured velocity vectors on the 45 x 45 km grid
 366 for radius r from the vortex center < 6010 km. Taking the azimuthal component of each vector,
 367 and knowing its r , we did two separate least squares fits, in both cases for the five a_n coefficients
 368 in Eq. (2), to get analytic expressions for $\partial\bar{\Phi}(r)/\partial r$ and $\bar{v}(r)$, respectively.

$$369 \quad \frac{\bar{v}^2}{r} + 2\Omega\bar{v} = -\frac{\partial\bar{\Phi}}{\partial r}, \quad \bar{\zeta} = \frac{\partial(r\bar{v})}{r \partial r}, \quad \bar{v} = \sum_1^4 a_n r^n + \frac{a_5 r}{(r^2 + r_0^2)} \quad (2)$$

371 For a good fit, the parameter r_0 must be close to the radius of the velocity maximum. It was
 372 chosen to be 1060 km for $\partial\bar{\Phi}/\partial r$ and 1200 km for \bar{v} . We analytically integrated the expression
 373 for cyclostrophic balance starting from $\bar{\Phi} = 0$ at $r = 0$ to get $\bar{\Phi}(r)$ in Figure 4, and we analytically
 374 differentiated the expression for velocity to get $\bar{\zeta}(r)$. See the SI for details.

375
 376
 377
 378 **Acknowledgments**
 379

380 This research was carried out at the California Institute of Technology under a contract with the
381 National Aeronautics and Space Administration (NASA), Grant/Cooperative Agreement Number
382 80NSSC20K0555, and a contract with the Juno mission, which is administered for NASA by the
383 Southwest Research Institute. CL was supported by the 51 peg b Postdoctoral Fellowship.
384 JIRAM was supported by the Italian Space Agency through ASI-INAF agreements n. I/010/10/0,
385 2014-050-R.0, 2016-23-H.0 and 2016-23-H.1-2018. AA, AM, DG, and FT were supported by
386 INAF. CP and GS were supported by ASI. LS is funded by the Scripps Institution of
387 Oceanography Postdoctoral Fellowship.
388

389 **Data Availability**

390 JIRAM data are available at the Planetary Data System (PDS) online ([https://pds-](https://pds-atmospheres.nmsu.edu/data_and_services/atmospheres_data/JUNO/jiram)
391 [atmospheres.nmsu.edu/data_and_services/atmospheres_data/JUNO/jiram](https://pds-atmospheres.nmsu.edu/data_and_services/atmospheres_data/JUNO/jiram)). Data products used in
392 this report include: calibrated, geometrically controlled, radiance data mapped onto an
393 orthographic projection centered on the north pole; velocity vectors derived from the radiance
394 data; and vorticity and divergence maps derived from the velocity data. These data products,
395 about 150 Mb in volume, are part of the SI.
396

397 **References**

- 398 1. Orton, G. S. *et al.* The first close-up images of Jupiter's polar regions: Results from the Juno mission
399 JunoCam instrument. *Geophys. Res. Lett.* **44**, 4599–4606 (2017).
- 400 2. Adriani, A. *et al.* Clusters of cyclones encircling Jupiter's poles. *Nature* **555**, 216–+ (2018).
- 401 3. Tabataba-Vakili, F. *et al.* Long-term tracking of circumpolar cyclones on Jupiter from polar
402 observations with JunoCam. *Icarus* **335**, UNSP 113405 (2020).
- 403 4. Adriani, A. *et al.* Two-year observations of the Jupiter polar regions by JIRAM on board Juno. *J.*
404 *Geophys. Res.* (2020) doi:DOI: 10.1029/2019JE006098201.
- 405 5. Grassi, D. *et al.* First Estimate of Wind Fields in the Jupiter Polar Regions From JIRAM-Juno Images. *J.*
406 *Geophys. Res.-Planets* **123**, 1511–1524 (2018).
- 407 6. Mura, A., Adriani, A. & Bracco, A. Oscillations and stability of the Jupiter polar cyclones. *Nature*
408 *Astronomy* (2021).

- 409 7. Li, C., Ingersoll, A. P., Klipfel, A. P. & Brettle, H. Modeling the stability of polygonal patterns of
410 vortices at the poles of Jupiter as revealed by the Juno spacecraft. *Proc. Natl. Acad. Sci. U. S. A.* **117**,
411 24082–24087 (2020).
- 412 8. Scott, R. K. Polar accumulation of cyclonic vorticity. *Geophys. Astrophys. Fluid Dyn.* **105**, 409–420
413 (2011).
- 414 9. O’Neill, M. E., Emanuel, K. A. & Flierl, G. R. Polar vortex formation in giant-planet atmospheres dues
415 to moist convection. *Nature Geoscience* **8**, 523-U118 (2015).
- 416 10. O’Neill, M. E., Emanuel, K. A. & Flierl, G. R. Weak Jets and Strong Cyclones: Shallow-Water Modeling
417 of Giant Planet Polar Caps. *J. Atmos. Sci.* **73**, 1841–1855 (2016).
- 418 11. Brueshaber, S. R., Sayanagi, K. M. & Dowling, T. E. Dynamical regimes of giant planet polar vortices.
419 *Icarus* **323**, 46–61 (2019).
- 420 12. Orton, G. S. & Yanamandra-Fisher, P. A. Saturn’s Temperature Field from High-Resolution Middle-
421 Infrared Imaging. *Science* **307**, 696–698 (2005).
- 422 13. Dyudina, U. A. *et al.* Dynamics of Saturn’s south polar vortex. *Science* **319**, 1801–1801 (2008).
- 423 14. Dyudina, U. A. *et al.* Saturn’s south polar vortex compared to other large vortices in the Solar
424 System. *Icarus* **202**, 240–248 (2009).
- 425 15. Hueso, R. *et al.* Jupiter cloud morphology and zonal winds from ground-based observations before
426 and during Juno’s first perijove. *Geophys. Res. Lett.* **44**, 4669–4678 (2017).
- 427 16. Sommeria, J., Meyers, S. & Swinney, H. Laboratory Model of a Planetary Eastward Jet. *Nature* **337**,
428 58–61 (1989).
- 429 17. Allison, M., Godfrey, D. & Beebe, R. A Wave Dynamic Interpretation of Saturns Polar Hexagon.
430 *Science* **247**, 1061–1063 (1990).
- 431 18. Aguiar, A. C. B., Read, P. L., Wordsworth, R. D., Salter, T. & Yamazaki, Y. H. A laboratory model of
432 Saturn’s North Polar Hexagon. *Icarus* **206**, 755–763 (2010).

- 433 19. Sanchez-Lavega, A. *et al.* The long- term steady motion of Saturn’s hexagon and the stability of its
434 enclosed jet stream under seasonal changes. *Geophysical Research Letters* **41**, 1425–1431 (2014).
- 435 20. Morales-Juberias, R., Sayanagi, K. M., Dowling, T. E. & Ingersoll, A. P. Emergence of polar-jet
436 polygons from jet instabilities in a Saturn model. *Icarus* **211**, 1284–1293 (2011).
- 437 21. Mied, R. & Lindemann, G. Propagation and Evolution of Cyclonic Gulf-Stream Rings. *J. Phys.*
438 *Oceanogr.* **9**, 1183–1206 (1979).
- 439 22. Chassignet, E. & Cushmanroisin, B. On the Influence of a Lower Layer on the Propagation of
440 Nonlinear Oceanic Eddies. *J. Phys. Oceanogr.* **21**, 939–957 (1991).
- 441 23. Chan, J. & Williams, R. Analytical and Numerical-Studies of the Beta-Effect in Tropical Cyclone
442 Motion .1. Zero Mean Flow. *J. Atmos. Sci.* **44**, 1257–1265 (1987).
- 443 24. Oruba, L., Lapeyre, G. & Riviere, G. On the Poleward Motion of Midlatitude Cyclones in a Baroclinic
444 Meandering Jet. *J. Atmos. Sci.* **70**, 2629–2649 (2013).
- 445 25. Ingersoll, A. & Cuzzi, J. Dynamics of Jupiters Cloud Bands. *J. Atmos. Sci.* **26**, 981+ (1969).
- 446 26. Limaye, S. Jupiter - New Estimates of the Mean Zonal Flow at the Cloud Level. *Icarus* **65**, 335–352
447 (1986).
- 448 27. Li, L. M. *et al.* Life cycles of spots on Jupiter from Cassini images. *Icarus* **172**, 9–23 (2004).
- 449 28. Garcia-Melendo, E., Perez-Hoyos, S., Sanchez-Lavega, A. & Hueso, R. Saturn’s zonal wind profile in
450 2004-2009 from Cassini ISS images and its long-term variability. *Icarus* **215**, 62–74 (2011).
- 451 29. Dowling, T. A Relationship Between Potential Vorticity and Zonal Wind on Jupiter. *J. Atmos. Sci.* **50**,
452 14–22 (1993).
- 453 30. Rhines, P. Waves and Turbulence on a Beta-Plane. *J. Fluid Mech.* **69**, 417–443 (1975).
- 454 31. Kaspi, Y. *et al.* Jupiter’s atmospheric jet streams extend thousands of kilometres deep. *Nature* **555**,
455 223+ (2018).
- 456 32. Galanti, E. Constraints on the latitudinal profile of Jupiter’s deep jets. **submitted**, (2021).

- 457 33. Heimpel, M., Gastine, T. & Wicht, J. Simulation of deep-seated zonal jets and shallow vortices in gas
458 giant atmospheres. *Nature Geoscience* **9**, 19-+ (2016).
- 459 34. Yadav, R. K., Heimpel, M. & Bloxham, J. Deep convection-driven vortex formation on Jupiter and
460 Saturn. *Sci. Adv.* **6**, eabb9298 (2020).
- 461 35. Adriani, A. *et al.* JIRAM, the Jovian Infrared Auroral Mapper. *Space Sci. Rev.* **213**, 393–446 (2017).
- 462 36. Gonzalez, R. C. & Woods, R. E. *Digital Image Processing*. (Pearson, 2016).
- 463 37. Garcia-Ortega, E., Lopez, L. & Sanchez, J. L. Diagnosis and sensitivity study of two severe storm
464 events in the Southeastern Andes. *Atmos. Res.* **93**, 161–178 (2009).
- 465 38. Marion, G. R. & Trapp, R. J. The Dynamical Coupling of Convective Updrafts, Downdrafts, and Cold
466 Pools in Simulated Supercell Thunderstorms. *J. Geophys. Res.-Atmos.* **124**, 664–683 (2019).
- 467 39. Merrill, R. A Comparison of Large and Small Tropical Cyclones. *Mon. Weather Rev.* **112**, 1408–1418
468 (1984).
- 469 40. Emanuel, K. A. *Atmospheric Convection*. (Oxford University Press, 1994).
- 470 41. Marshall, J. & Schott, F. Open-ocean convection: Observations, theory, and models. *Rev. Geophys.*
471 **37**, 1–64 (1999).
- 472 42. Little, B. *et al.* Galileo images of lightning on Jupiter. *Icarus* **142**, 306–323 (1999).
- 473 43. Gierasch, P. J. *et al.* Observation of moist convection in Jupiter’s atmosphere. *Nature* **403**, 628–630
474 (2000).
- 475 44. Gierasch, P., Conrath, B. & Magalhaes, J. Zonal mean properties of Jupiter’s upper troposphere from
476 Voyager infrared observations. *Icarus* **67**, 456–483 (1986).
- 477 45. Li, L. M., Ingersoll, A. P. & Huang, X. L. Interaction of moist convection with zonal jets on Jupiter and
478 Saturn. *Icarus* **180**, 113–123 (2006).
- 479 46. Thomson, S. I. & McIntyre, M. E. Jupiter’s Unearthly Jets: A New Turbulent Model Exhibiting
480 Statistical Steadiness without Large-Scale Dissipation*. *J. Atmos. Sci.* **73**, 1119–1141 (2016).

- 481 47. Ingersoll, A. P., Bolton, S. J. & Levin, S. M. Vertical momentum transport by atmospheric waves
482 explains Jupiter's stacked, oppositely-rotating Ferrel cells. *Geophysics Research Letters* **Submitted**,
483 (2021).
- 484 48. Duer, K., Gavriel, N. & Galanti, E. Evidence for multiple Ferrel cells on Jupiter. *Nature* **submitted**,
485 (2021).
- 486 49. Fletcher, L. N. Jupiter's temperate belt/zone contrasts revealed at depth by Juno microwave
487 observations. *J. Geophys. Res.: Planets* **(submitted)**, (2021).
- 488 50. Siegelman, L., Klein, P., Ewald, S. P., Ingersoll, A. P. & Young, W. R. Moist convection drives an
489 upscale energy transfer at Jupiter's high latitudes. *Nature* **Submitted**, (2021).
- 490 51. Sindoni, G. *et al.* Characterization of the white ovals on Jupiter's southern hemisphere using the first
491 data by the Juno/JIRAM instrument. *Geophys. Res. Lett.* **44**, 4660–4668 (2017).
- 492 52. Rubio, A. M., Julien, K., Knobloch, E. & Weiss, J. B. Upscale Energy Transfer in Three-Dimensional
493 Rapidly Rotating Turbulent Convection. *Phys. Rev. Lett.* **112**, 144501 (2014).
- 494 53. Novi, L., von Hardenberg, J., Hughes, D. W., Provenzale, A. & Spiegel, E. A. Rapidly rotating Rayleigh-
495 B\'enard convection with a tilted axis. *Phys. Rev. E* **99**, 053116 (2019).
- 496 54. Acton, C. H. Ancillary data services of NASA's Navigation and Ancillary Information Facility. *Planet*
497 *Space Sci.* **44**, 65–70 (1996).

498
499

Figures

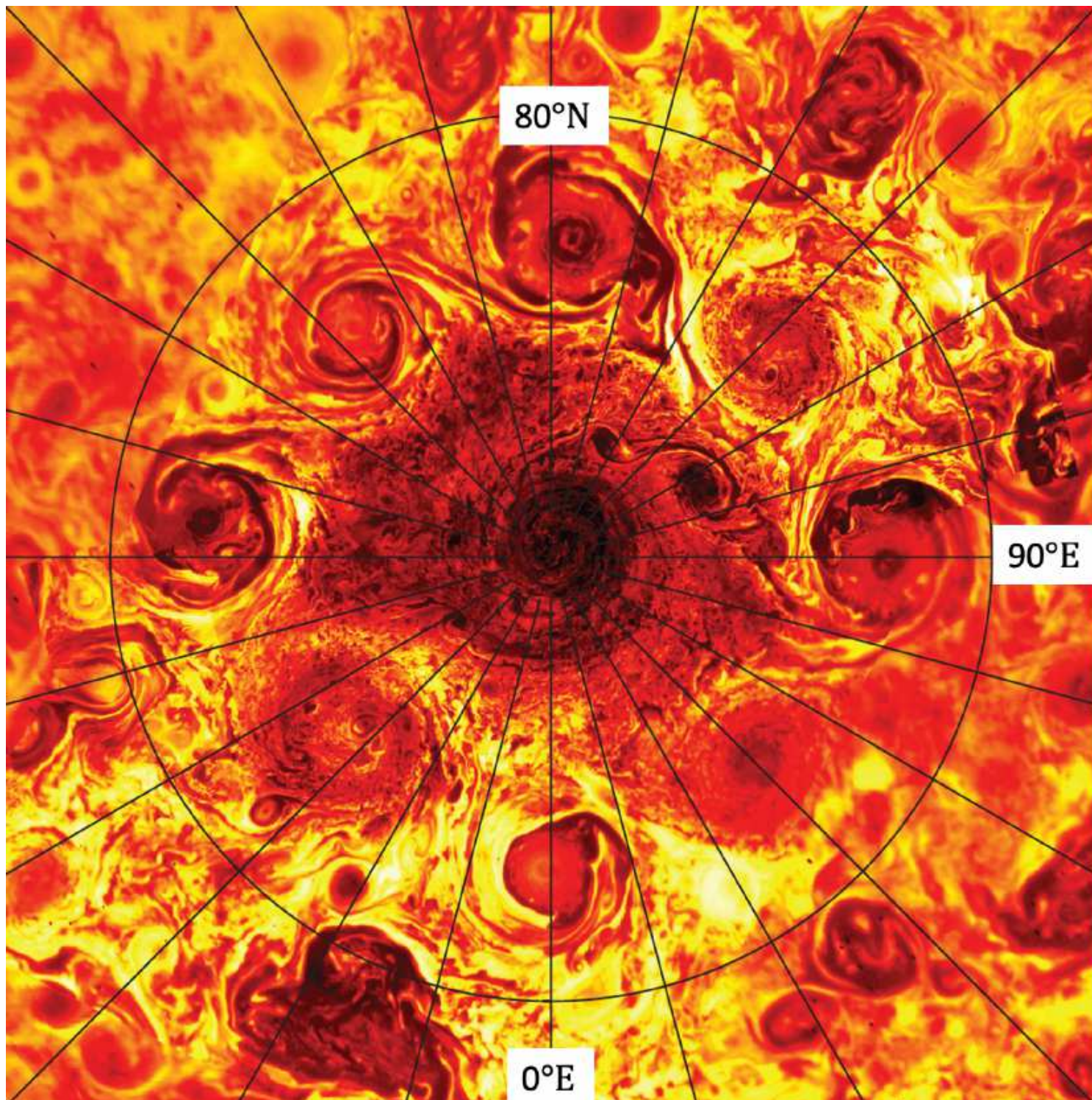


Figure 1

Infrared image of the northern hemisphere as seen by JIRAM 2. The circle at 80° latitude is about 12,000 km from the pole. The radiances have been corrected for nadir viewing, with bright yellow signifying greater radiance and dark red signifying lesser radiance. Because of these corrections and the non-linearity of the Planck function, one can only say that the average brightness temperature is somewhere

in the range 215-220 K. The figures shown in this paper cover the central cyclone and the two cyclones at 135° and 315° east longitude, respectively. The two dark features at 120-150° east, whose filaments spiral toward their centers in a clockwise direction, are anticyclones.

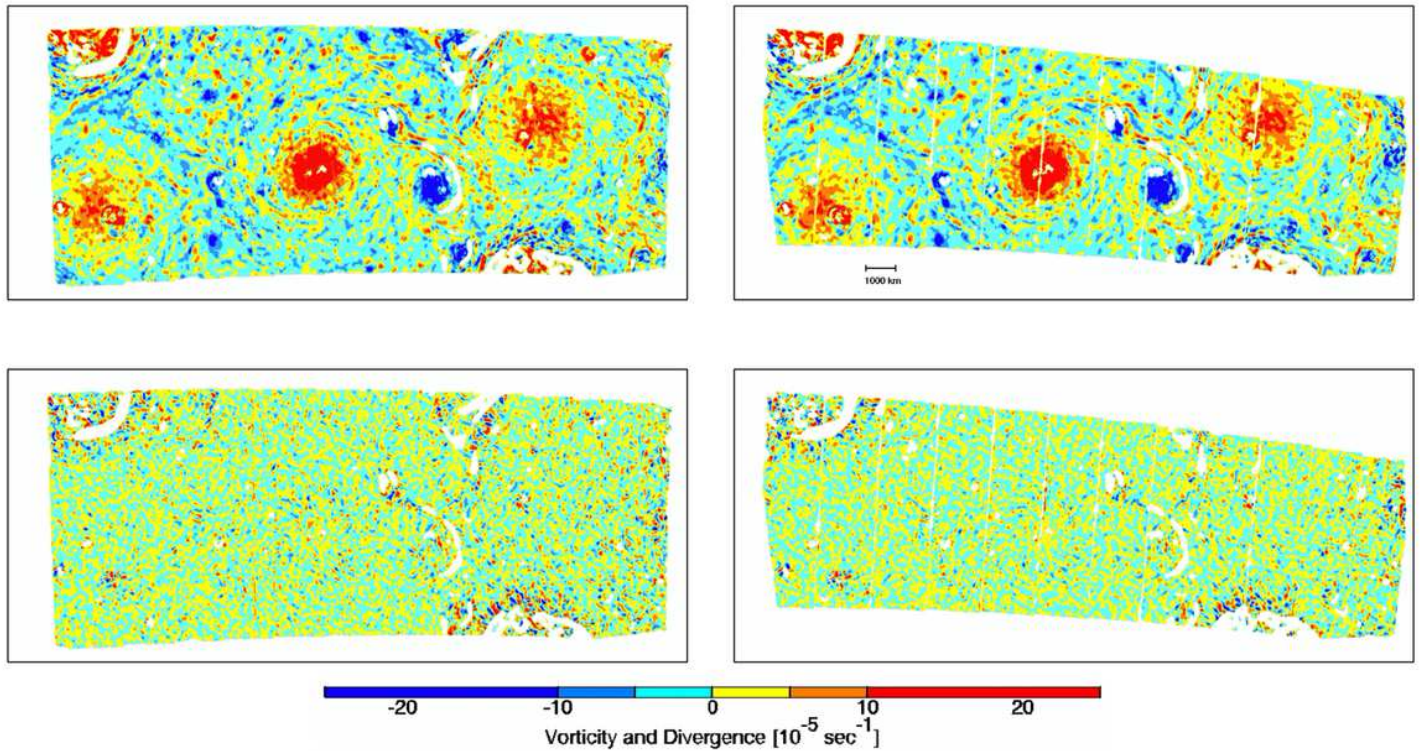


Figure 2

Vorticity (top row) and divergence (bottom row) derived from two determinations of the wind field using separate data (left and right), termed n0103 and n0204. The long dimension of each rectangle is $\sim 20,000$ km, and the smallest features are ~ 100 km in diameter. Each determination is derived from a series, each of which consists of 12 adjacent images laid side by side. The seams between the 12 images are visible as faint vertical lines. The white spaces are regions where the image entropy³⁶ was below a threshold needed for reliable cloud-tracked wind analysis. They cover 1.8% and 2.1% of the pixels in the left and right maps, respectively. For further information, see the Methods section

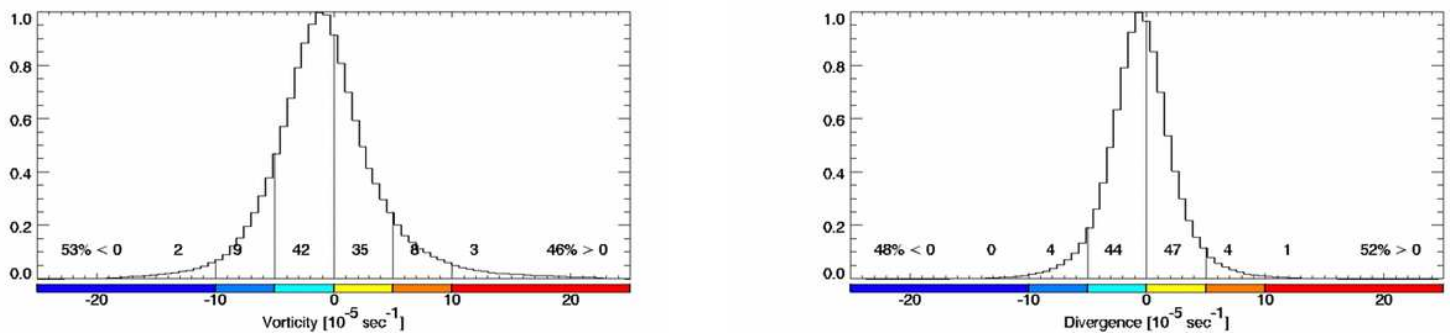


Figure 3

Histograms of vorticity (left) and divergence (right) for the maps shown in Figure 2. The vorticity and divergence scales are the same, and the colors are the same as those used in Figure 2. The number above each color bin is the percentage of pixels in that bin.

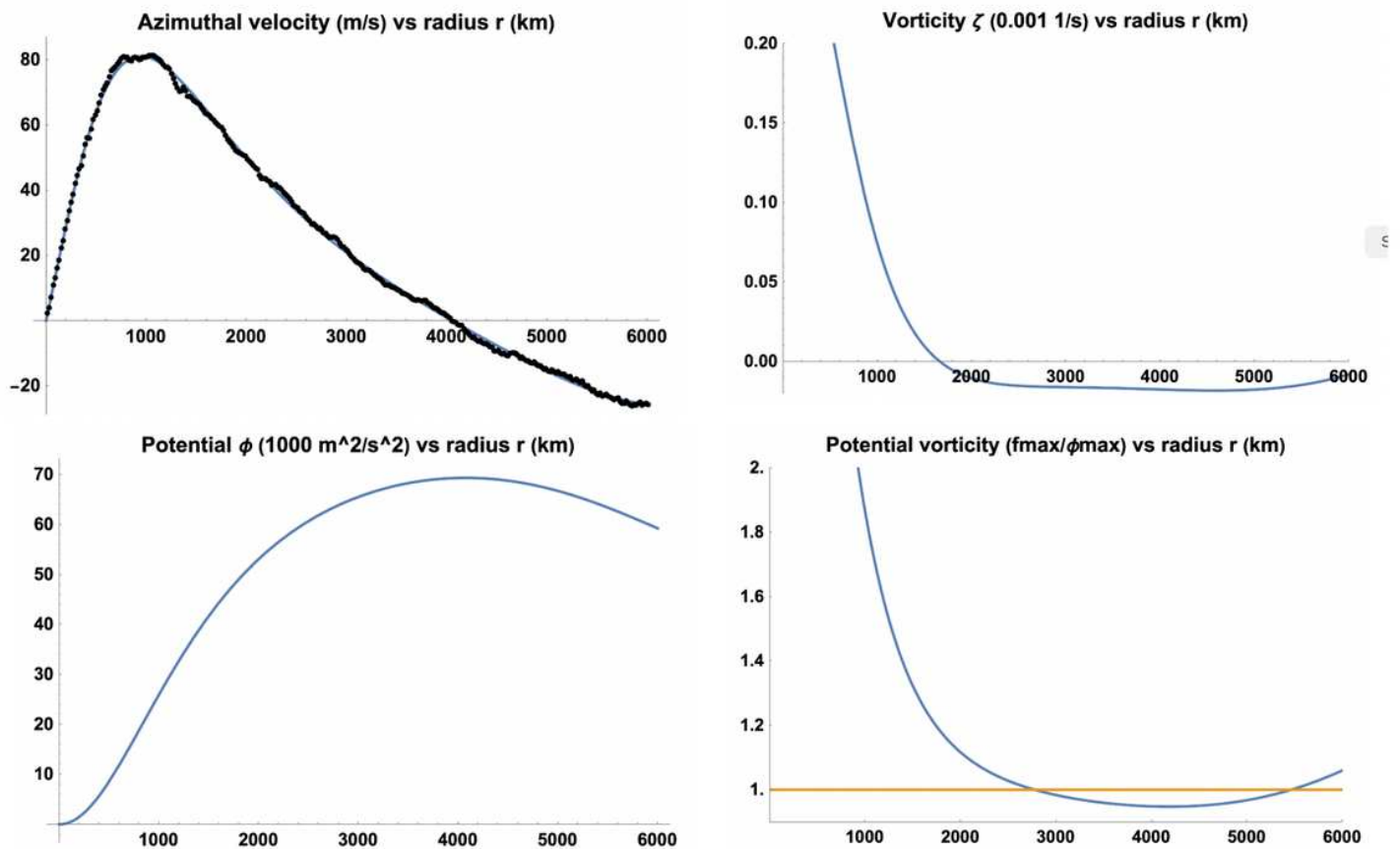


Figure 4

Mean azimuthal velocity and vorticity (top row) and mean gravitational potential and potential vorticity (bottom row). The fitted curve for velocity (blue) is almost covered by the data points (black). Please see manuscript .pdf for full caption.

Supplementary Files

This is a list of supplementary files associated with this preprint. Click to download.

- [SupplementaryInformation40221.pdf](#)
- [figs1polarvortexblink.pdf](#)
- [figs2entropymasksremoved.pdf](#)